Materials & Design 225 (2023) 111467

Contents lists available at ScienceDirect

Materials & Design

journal homepage: www.elsevier.com/locate/matdes

Novel bio-inspired 3D porous scaffold intended for bone-tissue engineering: Design and *in silico* characterisation of histomorphometric, mechanical and mass-transport properties

Sergio Gómez González [a], Maria Daniela Vlad [b,c], José López López [a], Enrique Fernández Aguado [a,*]

[a] Research Group of Interacting Surfaces in Bioengineering and Materials Science (InSup), Technical University of Catalonia (UPC), Avda. Diagonal, 647, 08028 Barcelona, Spain
[b] Faculty of Medical Bioengineering, "Grigore T. Popa" University of Medicine and Pharmacy from Iasi, Str. Kogălniceanu, 9-13, 700454 Iasi, Romania
[c] TRANSCEND Research Centre, Regional Institute of Oncology, Str. G-ral Henri Mathias Berthelot, 2-4, 700483 Iasi, Romania

HIGHLIGHTS

- Novel porous scaffolds have been developed that mimic the mechanical and fluid properties of cancellous bone.
- The new porous scaffolds have high specific surface area and controllable surface curvatures.
- The design methodology is suitable for modifying the internal microstructure of computed tomography medical images.
- The design methodology allows for the development of bone-like scaffolds with continuous but graduated material properties.
- The properties of the scaffolds depend on the direction of their trabeculae, their total porosity, and their bone surface.

GRAPHICAL ABSTRACT

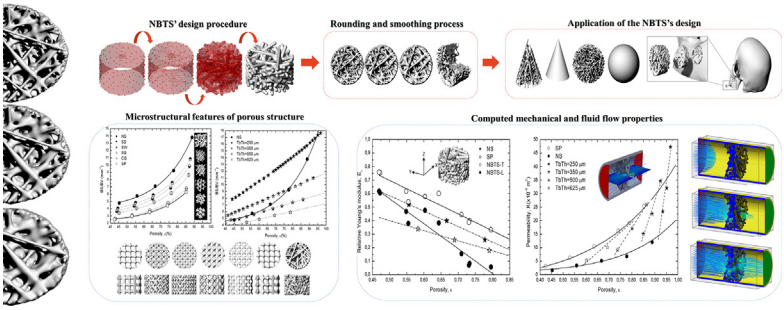

ARTICLE INFO

Article history:
Received 9 June 2022
Revised 4 October 2022
Accepted 5 December 2022
Available online 6 December 2022

Keywords:
Bone tissue engineering
Porous scaffold's computer-aided design
Computational fluid dynamics
Permeability
Tortuosity
Histomorphometry

ABSTRACT

The design of novel biomimetic bone tissue scaffolds (BTS) using computer aided design (CAD) technology is challenging additive manufacturing technologies. At the microstructure level, BTS should mimic bone histomorphometry and assure optimum mass transport and mechanical properties. In this study, a novel BTS has been designed, by using a parametric and variational CAD method, to model a bio-inspired and interconnected porous structure. The mechanical (elastic modulus) and the fluid mass transport (permeability) properties have been computed and compared to other implicit surfaces modelling scaffolds. The results showed that the new BTS could be tuned during the design stage to match the microstructure and the histomorphometry properties of trabecular bone. Those with porosities between 0.7 and 0.9 and highly smooth curvatures were the most appropriates. The new BTS, once appropriately designed, could be made/manufactured by 3D printing technology with an internal microstructure mimicking the local bone properties of the selected bone volumes of interest, for example, those coming from computed tomography medical images.

* Corresponding author at: Department of Materials Science and Engineering, Technical University of Catalonia (UPC), Avda. Diagonal 647, E-08028-Barcelona, Spain.
E-mail address: enrique.fernandez@upc.edu (E.F. Aguado).

https://doi.org/10.1016/j.matdes.2022.111467
0264-1275/

1. Introduction

In orthopaedic surgery, autografts and allografts are common options used for bone repair. However, because there have been reported cases of pain, infection and immune rejection the attention has been directed towards the use of synthetic bone-like porous scaffolds that at present lack the sufficient mechanical strength and vascularization [1,2]. For this reason, in order to ensure similar bone properties, it is necessary that future designs of bone tissue scaffolds (BTS) mimic the natural inorganic bone microarchitecture (i.e., porosity, pores sizes and shapes, internal trabecular structure, trabecular interconnection and orientation, etc.). In doing so, it is expected that cell adhesion, cell migration, cellular nutrients diffusion and new bone apposition (i.e., osteoconduction) should improve [3–11]. In this sense, it is known that high porosity and large pore size benefit the permeability of the scaffold (in consequence, cell migration and nutrient mass transport) but they go against its mechanical properties [12–14]. In fact, there is no consensus on the best form of porosity because there are many other microstructural characteristics that also affect the *in vitro* and/or *in vivo* behaviour of the scaffold, as well as its mechanical and rheological properties [15]. For example, recent studies indicate that the rate of bone regeneration increases with curvature and is much higher on concave surfaces than on flat and convex surfaces. There is evidence that shows that cells present different attachment behaviour to concave and to convex spherical surfaces ranging from 250 to 750 μm of diameter (approximately, 2–3 times mesenchymal stem cell's size). Cells in concave spherical surfaces showed an upward lift of the cell body and migrated faster compared to cells in flat or convex surfaces. Convex surfaces led to flattened cell morphology and promoted osteogenic differentiation [16,17].

In this scenario, several strategies have been proposed to design BTS by using computer aided design (CAD) methods involving periodic porous structures (solid primitives through Boolean operations), space-filling curves (micro extrusion of a small filament) or implicit surface modelling (ISM) with and without pore sizes gradients [18–20]. For example, ISM uses trigonometric functions to maximise the surface to volume ratio of the scaffold; this is known to have positive effects on cell migration and tissue ingrowth [21–23]. In addition, medical image processing of computed tomography (CT) and micro-CT (μCT) has been used as the basis to build three-dimensional (3D) biomimetic scaffolds with irregular porous structure [24,25]. More recently, irregular porous scaffolds have been designed by stochastic and Voronoi tessellation methods to mimic the randomness of natural bone with CAD-parametric software. In this approach, some histomorphometric indices such as the trabecular thickness, the total porosity and the bone-surface area are controlled at the start of the design process [26–28].

In this article, a novel approach, using parametric CAD software, to the design of irregular porous BTS with high values of bone-surface area is presented. The article shows different designs of novel BTS having its interconnected porosity, its trabecular thickness and its pore shape and distribution, properly controlled. It also shows different ways to fit the new BTS to any external volume shape and how this can be filled by previous designed irregular porous internal microstructure. Additionally, the paper presents a comparative computation study of both, mechanical and fluid properties, over a range of different porosities between the new proposed BTS and some of the most used ISM scaffolds.

However, it should be highlighted that the objectives of this article were fixed beforehand: a) to explain the design procedure followed to build the new porous bone-like scaffolds; b) to compute by mathematical modelling the histomorphometry, the mechanical (elasticity) and the rheological properties of the new porous bone-like scaffolds; and c) to compare the theoretical results obtained for the new designs with other published experimental and theoretical data obtained with other well established ISM bone-like porous scaffolds.

It is expected that the new proposed BTS, in combination with present computer-assisted tissue engineering and additive manufacturing technologies, should help to produce better biomimetic scaffolds with optimum mechanical and biological properties, similar to those that are ideal for bone tissue engineering applications [10,17,29,30].

2. Materials and methods

2.1. Design of porous scaffolds

The novel bone tissue scaffolds (NBTS) were designed with the software *Grasshopper*^{TM} (www.grasshopper3d.com) as follows: a) first, an arbitrary portion of space in the form of a cylinder of appropriate dimensions was created (Ø=10 mm, L = 6 mm) to test the new design concept; b) then, a certain number of random points (NRP) were inserted only along the lateral surface of this first cylinder (Fig. 1.a); c) then, the points were randomly connected by straight lines (Fig. 1.b.); d) then, the resulting straight-lines generated inside the first cylinder were also transformed into small cylinders of suitable diameters (Fig. 1.c); and finally, e) the interconnected surfaces of the resulting cylinders were meshrounded and smoothed (Fig. 1.d) with the software *Cocoon*^{TM} (www.bespokegeometry.com/2015/07/22/cocoon/). Furthermore, the radius of these internal cylinders was gradually increased to obtain similar scaffolds with different trabecular thicknesses and porosities (see, Fig. 1.e-f). In this sense, it is important to point out that the entire design procedure is not limited to a particular external geometry figure, but can also be used to fill any portion of space (of any three-dimensional geometry) and/or anatomical defect of interest (see, Fig. 2.a-c). The cylinder shape was selected as a proof of concept for the new designs because it is a standard sample of geometry often used for testing and calculating mechanical (finite element analysis, FEA) and fluid properties (computing fluid dynamics, CFD) of materials, thus serving as a good validation model. Furthermore, long bones have a cylindrical geometry, with a dense external microstructure (cortical bone) and a porous internal microstructure (trabecular bone). For all these reasons, the cylindrical geometry was considered the most appropriate for this study.

In consequence, for comparison purposes (see, Fig. 3), similar cylinders as those proposed in Fig. 1, but designed with the open-software *K3DSurf* (www.k3dsurf.sourceforge.net), were also filled with known implicit surface models (Neovius Surface (NS), Schwarz's Diamond (SD), Schwarz's W (SW), Shoen's Gyroid (SG), Cylinder Grid (CG) and Schwarz's Primitive (SP)). All the models had values of porosity (ε), trabecular thickness (Tb.Th) and bone surface (BS) in the intervals of $0.4 < \varepsilon < 0.9$, $230 < Tb.Th < 1330$ μm and $430 < BS < 1230$ mm^2, respectively.

2.2. Characterization of mechanical properties

First, cubes of interest of a 4 mm side were extracted with the *Boolean split* command (*Rhinoceros, Robert McNeel & Associates*) from the centre of the scaffolds (Fig. 4.a) and converted to closed solid poly-surfaces with the *Meshtonurbs* command (*Rhinoceros, Robert McNeel & Associates*). Then, the STL files were exported to *SolidWorks Simulation* as solid geometry for uniaxial compression computation of the models along both, the longitudinal (Z) and the two transverse directions (X and Y) to account for anisotropy behaviour (Fig. 4.b). Additionally, to assure optimum mesh of the

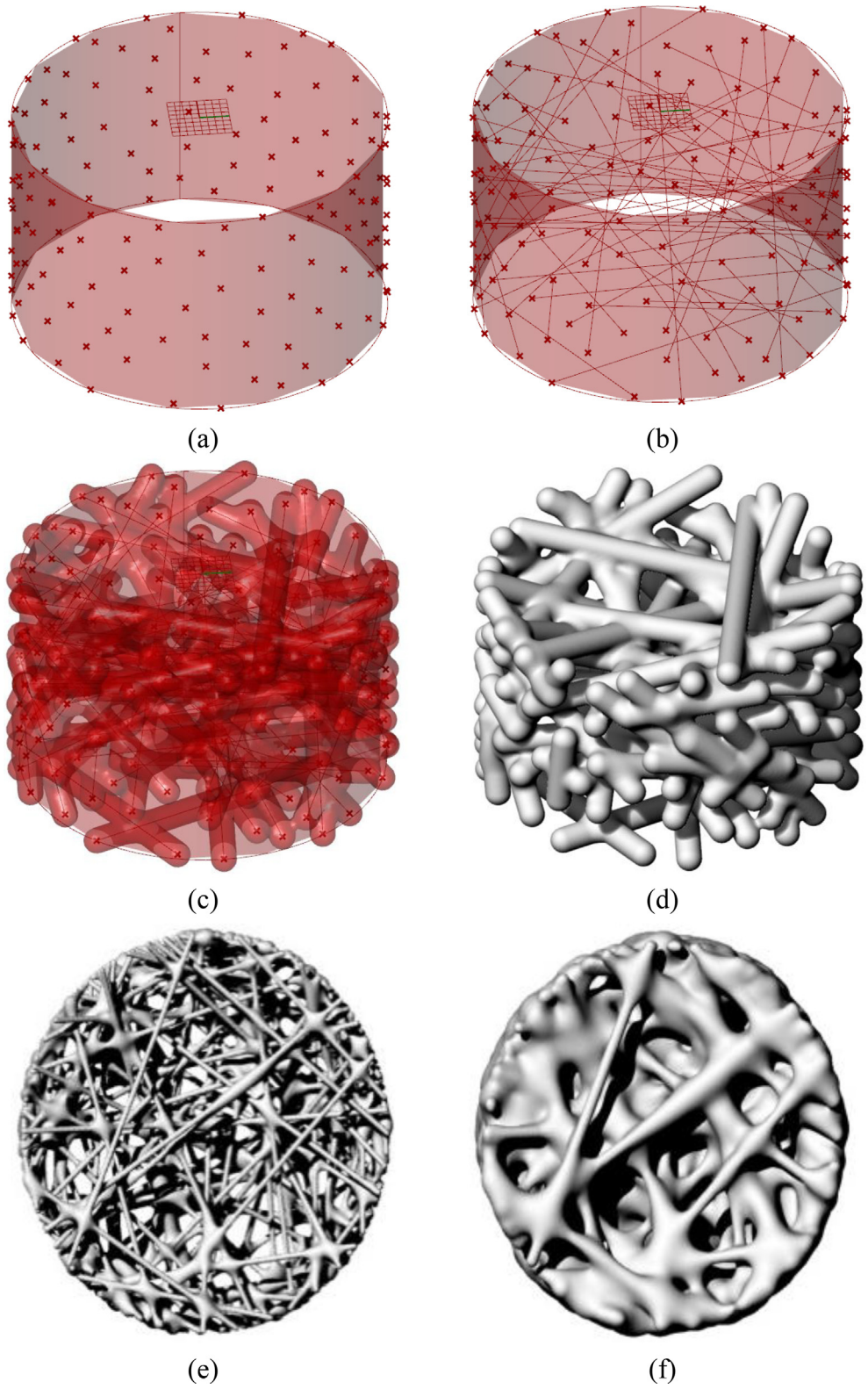

Fig. 1. NBTS' design procedure tested on an arbitrary portion of space in the form of a cylinder: a) Cylinder with N-random points distributed on its lateral surface; b) Interconnection of random points to create N/2-straigth lines; c) Conversion of straight lines into cylinders of fixed diameter; d) Rounding and smoothing process of interconnecting cylinders' surfaces; e-f) Transversal view of twin scaffolds with different trabecular thickness and so, different porosities.

models, some degenerated faces and edges were repaired with the software *Netfabb* (https://www.autodesk.com). The material selected for computation was poly(D,L-lactide) which is often used for testing 3D printed bone tissue models. Thus, these are the material properties that were selected: Young's modulus, E_s = 3.3 GPa; Poisson's ratio, ν = 0.3; and, density, ρ = 1.3 g/cm^3. Computation boundary conditions were: displacement for the top face (maximum engineering strain, ε_{max} = 1%); fixation

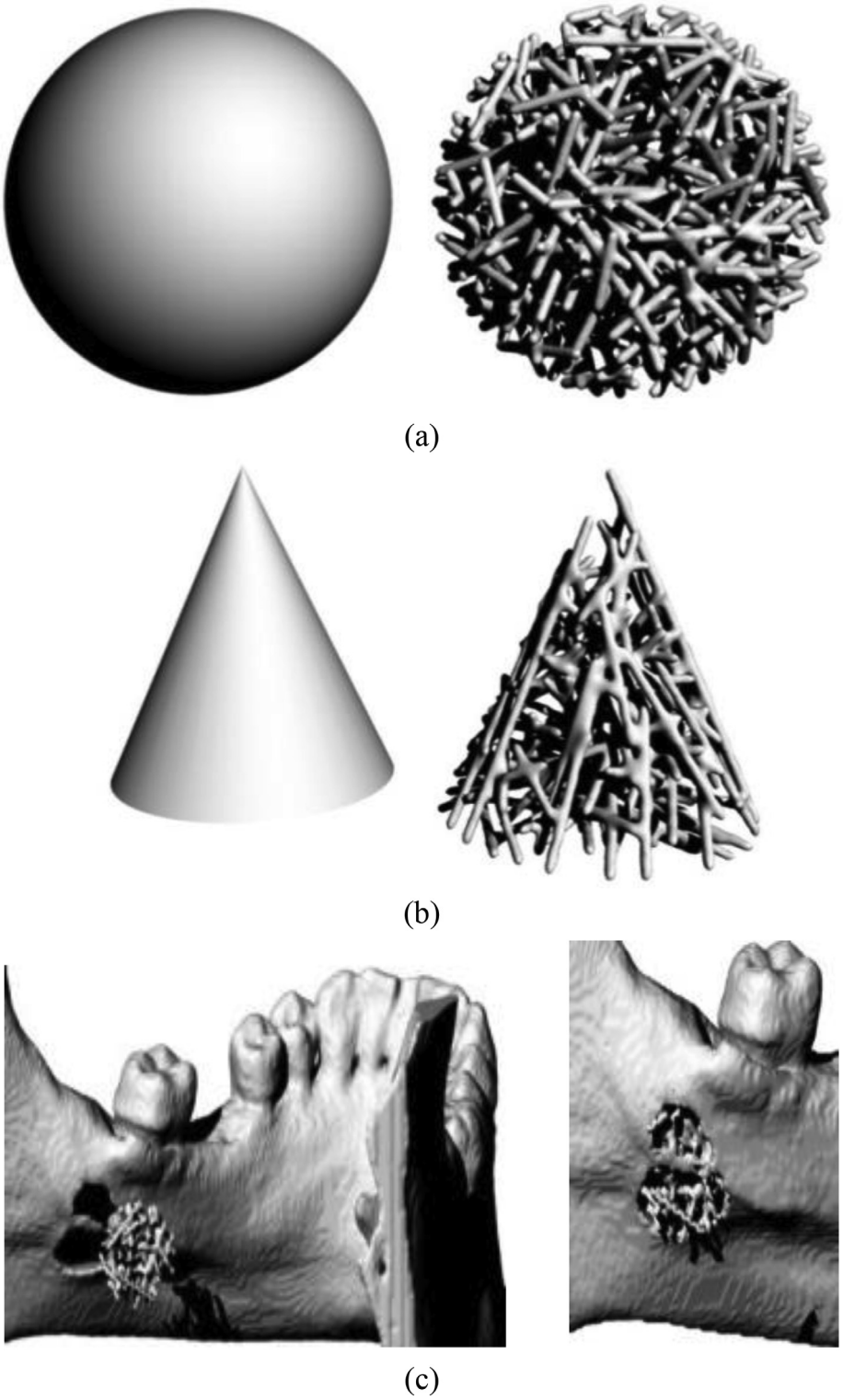

Fig. 2. Application of the NBTS's design procedure to different external geometries and needs: a) sphere; b) cone; c) bone defect in human mandible.

for the bottom-face; and, symmetry for the rest of the faces [27,28,31]. The simulations, done for all the models (Fig. 4.c), computed average values for the true reaction stress at their bottom surface (σ_{av}), the von Mises stress (σ_{vM}) and the strain or displacement field (ε). Then, the Young's modulus of each porous scaffold (E_p) was calculated as the ratio between the σ_{av} obtained at the maximum axial engineering strain and this same strain (i.e., ε_{max} = 1%). The relative Young's modulus of the models (E_r), which is dimensionless by definition, was calculated as the ratio between the E_p and the E_s.

Accurate mechanical computation results needed>$2.3x10^6$ mesh elements on average (maximum time for meshing, 120 min; minimum time for analysis, 20 min; Hewlett Packard Workstation: Intel Core i5, 96 GB RAM).

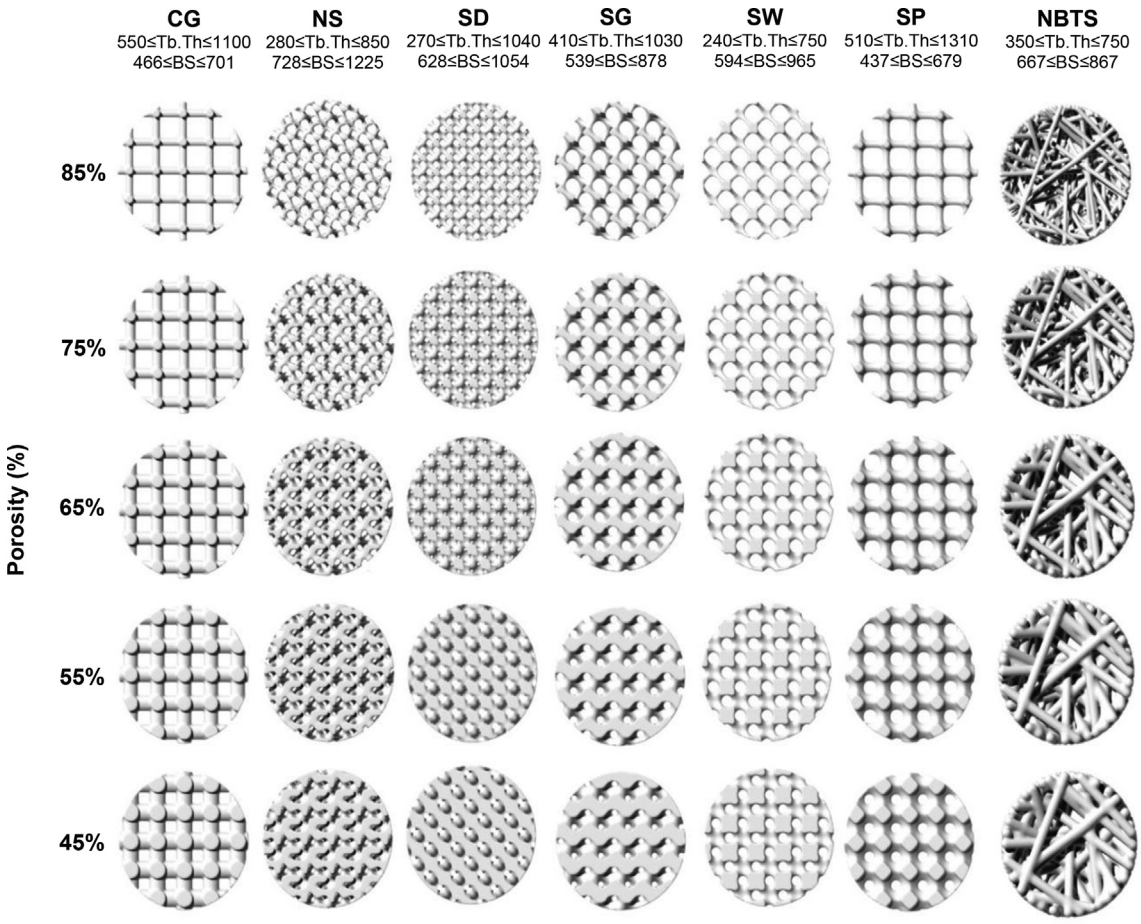

Fig. 3. Implicit surface models (i.e., NS, SD, SW, SG, CG and SP) and the new NBTS model under study. The NBTS model shown had a number of random points, NRP, of 400. The models are classified according to their equivalent porosities, which vary from 0.45 to 0.85. Furthermore, the intervals of variation of trabecular thickness, Tb.Th, and bone surface, BS, for each model, are also shown (see the text for code identifications).

2.3. Characterization of fluid flow properties

First, the designed scaffolds were checked with the *Meshrepair* command (*Rhinoceros, Robert McNeel & Associates*) to assure optimum mesh. Then, the files were saved as STL (Stereolithography) format and exported for fluid flow properties computation to software *SolidWorks Simulation*. The computation process was performed under laminar and stationary boundary conditions following a similar permeability setup as that used by several authors [27,31–34] where the scaffolds are placed at the centre of a cylinder ($Ø_c$ = 10 mm, L_c = 25 mm) and a blood simulating fluid is allowed to pass through it (Fig. 5). Computations in the present study were performed under a static outlet pressure of 101325 Pa (i.e., atmospheric pressure), a constant inlet velocity of $V_0 = 1x10^{-3}$ m/s, at 37 °C and setting for the fluid a dynamic viscosity of $\mu_d = 3x10^{-3}$ Pa·s (i.e., the dynamic viscosity of blood at 37 °C). This established setup allowed the calculation of the average pressure drop between the flow inlet and outlet faces of the scaffolds, $\Delta P_{i\text{-}o}$(Pa), as well as the average flow velocity, V_f(m/s), shear rate, $\gamma(s^{-1})$, shear stress, τ(Pa), and vorticity, ω (s^{-1}), of the fluid along the scaffolds' length. It should be noted that the pressure value selected for the outlet face (1 atm) is an arbitrary but convenient value to compute the pressure at the inlet face (Fig. 5). From this point of view, the only value of interest is the pressure difference between the inlet and outlet faces, $\Delta P_{i\text{-}o}$(Pa). This is the necessary data that allows calculating the intrinsic permeability, k(m^2), of the scaffolds according to Darcy's law. [27,31].

Additionally, a particle tracing analysis was performed to compare the 3D internal complexity of the scaffolds. For this, the average length travelled by 20 particles (Ø=10 μm; ρ = 1 g/cm^3) moving along the established laminar and stationary flow field was computed. It was assumed that particles reflected ideally against the cylinder walls. In addition, possible effects due to gravitation, accretion and erosion were not considered. With this setup, the tortuosity (τ, dimensionless by definition) of the scaffold was obtained as the ratio between the average length of the path followed by the particles through the scaffold, λ, and its total length (i.e., L_s = 6 mm).

To assure convergence of the fluid computations, a minimum of $8x10^6$ mesh elements were needed, with 24 h required, on average, for every model mesh and computing (Hewlett Packard Workstation, Intel Core i5, 96 GB).

3. Results

3.1. Design of porous scaffolds

Table 1 collects, as an example, some basic data (Tb.Th, BS and BV (bone volume)) measured for the ISM and the NBTS scaffolds. ISM data do not have statistical variability. On the other hand, the mean values of BS and BV in the NBTS models showed deviations of less than 3% over samples of 3 replicates (data not shown). Consequently, the error propagated to other calculated parameters, that is, BS/BV and ε, was even less than 3%. Thus, due to this very

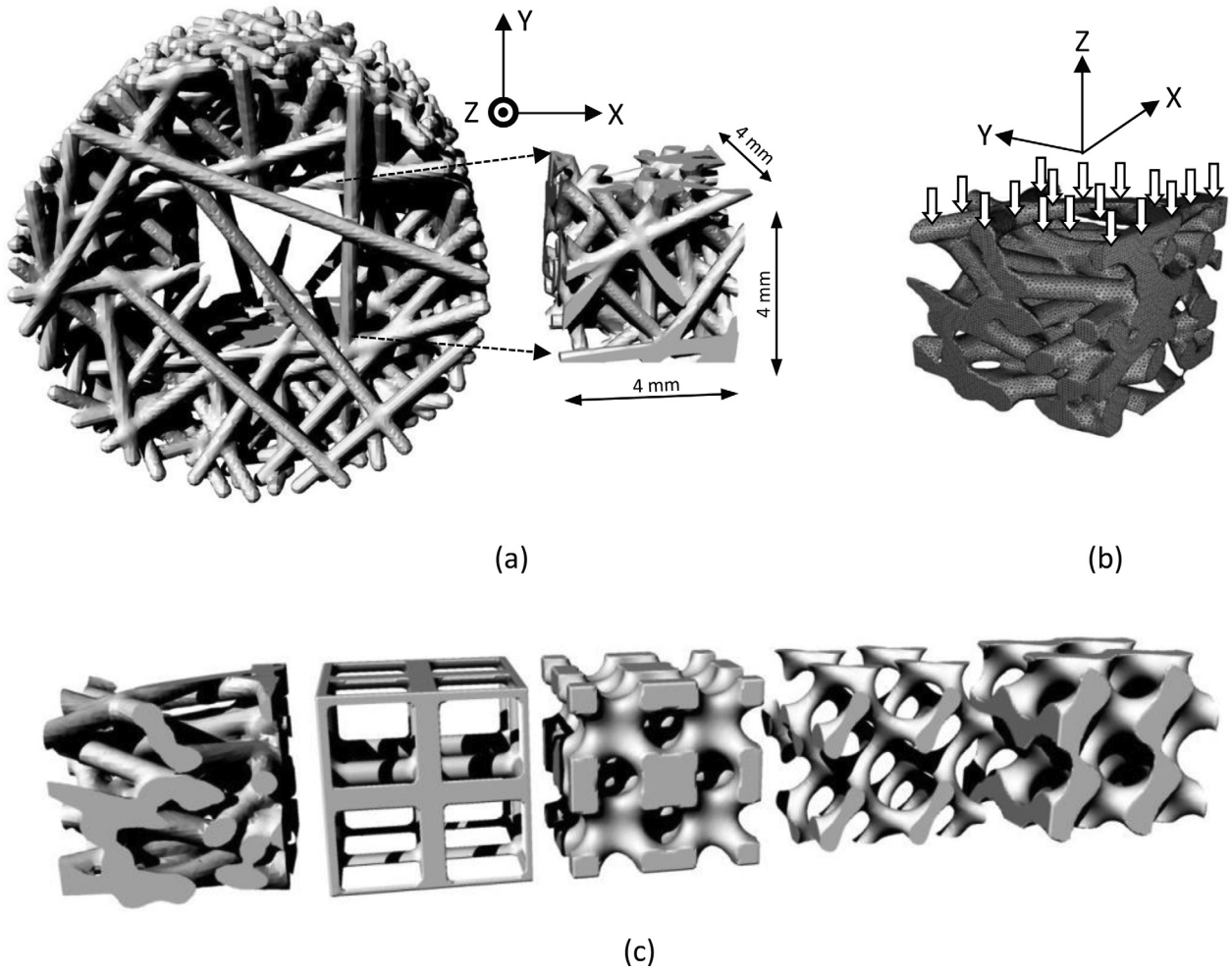

Fig. 4. Volume of interest selected for the calculation of the mechanical properties of the scaffolds. a) *Boolean split* operation of a cube of interest extracted from the centre of a NBTS scaffold; b) Solid STL file under uniaxial compression along the z-axis and on the x-y plane. c) Example of some models studied under compression (from left to right: NBTS, CG, SW, SG and NS).

small statistical variability, the data of Table 1 were mainly used to build Figs. 6 and 7 to clarify the main observed tendencies. Fig. 6 shows for each ISM scaffold the corresponding correlation between its specific surface ratio (i.e., BS/BV) and its porosity ($\varepsilon = 1 - BV/TV$). The models were fitted correctly to an exponential growth behaviour ($y = y_0 + A_1 \cdot e^{x/t_1}$). At zero porosity the BS/BV ratio approached the theoretical value of 0.73 mm^{-1} expected for the used cylindrical geometry ($Ø_s$ = 10 mm, L_s = 6 mm). The deviations from this value varied from 0.76 for the CG model to 1 for the NS model. All the models showed squared correlation coefficients, r^2, comprised from 0.9836 for the CG model to 0.9892 for the SW model. The scaffolds that showed the highest and lowest values of BS/BV ratio in the porosity interval of interest ($0.4 < \varepsilon < 0.9$) were the NS ($4.5 < BS/BV(mm^{-1}) < 14$) and the SP ($2.5 < BS/BV(mm^{-1}) < 7$) models, respectively. The values of BS/BV ratio for the other studied models were comprised between the NS and SP models (i.e., NS > SD > SW > SG > CG > SP). In general, the ISM models showed higher differences between their corresponding BS/BV ratios at higher than lower values of porosity. This is a normal trend when different exponential growth data fittings have the same theoretical or limit value at zero porosity (in this case, BS/BV = 0.73 mm^{-1}).

Additionally, Fig. 7a shows that for the new NBTS models the observed correlation between BS/BV and ε was linear. In this figure, the exponential growth observed in Fig. 6 for the implicit NS model (i.e., the one with the highest specific surface area) has also been included for comparison purposes. In this sense, Fig. 7a shows that the NBTS models have higher BS/BV ratio than the NS model when the diameter of the generated lines (Tb.Th) is lower than 500 μm. For example, the NBTS models having Tb.Th of 350 and 250 μm showed higher BS/BV values than the NS model in the porosity interval of ($0.4 < \varepsilon < 0.78$) and ($0.4 < \varepsilon < 0.94$), respectively. Moreover, Fig. 7b helps to visualize the microstructural differences between the NS and the NBTS models at some relevant coordinate points of Fig. 7a. For example, the top line shows the microstructures observed for equivalent 70% porosity models (left: NS; middle: Tb.Th = 350 μm; right: Tb.Th = 250 μm). Similarly, the down line shows the microstructures of the NBTS models that have the same specific surface area than their equivalent NS model, i.e., the intersection points between the NS exponential growth curve and the NBTS linear curves in Fig. 7a (left: Tb.Th = 500 μm, BS/BV ≅ 5.25 mm^{-1}, ε ≅ 52.5 %; middle: Tb.Th = 350 μm, BS/BV ≅ 9.25 mm^{-1}, ε ≅ 78 %; right: Tb.Th ≅ 250 μm, BS/BV ≅ 17 mm^{-1}, ε ≅ 94 %).

The design procedure can be completed with Fig. 8a, which shows how the specific surface area of the new models varies, for any selected trabecular thickness, with the number of random points seeded on the lateral surface of the selected cylindrical geometry (see, *2.1. Design of porous scaffolds*). This figure clearly shows that for any Tb.Th value, the BS/BV ratio decreases as the

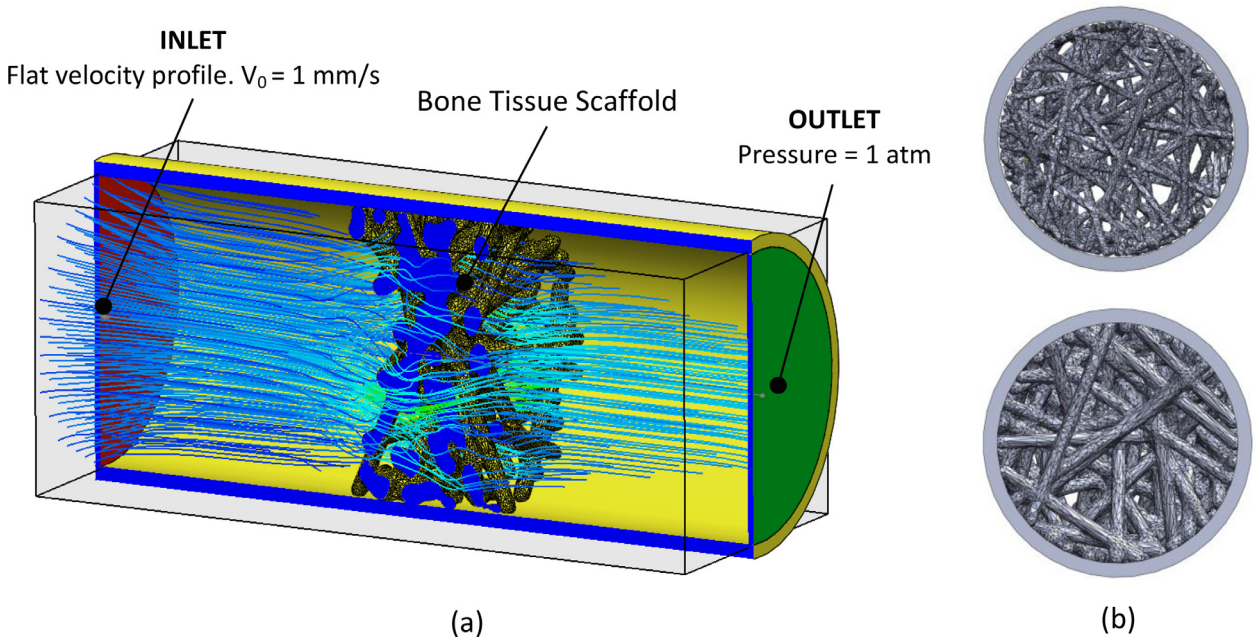

Fig. 5. Setup and boundary conditions for fluid flow and particles trace computations: a) Longitudinal section of the experimental set up: the studied scaffold (blue) is centred in a tube (yellow) of its same diameter (10 mm) but higher length (i.e, L_c = 25 mm *versus* L_s = 6 mm); the inlet (red) and the outlet (green) fluid flow surfaces are also shown; b) example of two scaffolds under a fluid flow study, in transversal view, with the same number of random points, NRP, but different trabecular thickness, Tb.Th (see the text for further explanations). (For interpretation of the references to colour in this figure legend, the reader is referred to the web version of this article.)

Table 1
Trabecular thickness (Tb.Th), bone surface (BS) and bone volume (BV) values measured for the ISM and NBTS scaffolds.

ISM scaffolds							
Scaffold	Tb.Th (μm)	**BS (mm^2)**	**BV (mm^3)**	**Scaffold**	Tb.Th (μm)	**BS (mm^2)**	**BV (mm^3)**
SD-1	270	628.35	58.08	SG-1	410	539.01	62.60
SD-2	420	818.69	108.63	SG-2	600	682.42	111.33
SD-3	540	948.61	162.03	SG-3	710	781.42	159.71
SD-4	660	1020.83	211.71	SG-4	870	845.34	208.96
SD-5	1040	1054.64	261.53	SG-5	1030	878.75	258.10
CG-1	550	466.87	69.16	SP-1	510	437.34	69.59
CG-2	740	577.16	120.49	SP-2	660	537.32	122.07
CG-3	930	644.86	171.37	SP-3	860	604.44	171.96
CG-4	1100	683.94	221.08	SP-4	1080	652.04	221.86
CG-5	1280	701.15	268.35	SP-5	1310	679.94	270.99
SW-1	240	594.32	60.31	NS-1	280	728.75	52.90
SW-2	390	776.80	113.07	NS-2	410	966.78	104.75
SW-3	510	880.85	164.18	NS-3	540	1108.11	156.53
SW-4	640	941.70	215.64	NS-4	670	1189.81	207.55
SW-5	750	965.77	264.46	NS-5	850	1225.19	257.52
NBTS scaffolds							
NGL	Tb.Th (μm)	**BS (mm^2)**	**BV (mm^3)**	**NGL**	Tb.Th (μm)	**BS (mm^2)**	**BV (mm^3)**
100	250	274.18	15.55	100	625	593.69	100.26
150		398.07	22.95	150		784.66	144.62
200		524.89	31.13	200		910.62	187.70
100	350	395.95	36.09	100	750	664.97	142.91
150		562.77	52.99	150		833.28	203.61
200		715.56	71.06	200		903.73	258.65
100	500	502.69	64.48	100	875	711.00	191.73
150		693.03	94.01	150		831.58	268.21
200		845.86	124.09	200		834.50	331.41

Note 1: SD, Schwarts Diamond; CG, Cylinder Grid; SW, Schwarts W; SG, Shoen Gyroid; SP, Schwarts Primitive; NS, Neovius' Surface; NGL, number of generating lines (NGL = 2NRP; NRP, number of random points). **Note 2:** BS and BV values allow to calculate the BS/BV ratio. **Note 3:** The Total Volume, TV, of each scaffold equals 150π, by definition; with this value, the corresponding indices BS/TV, BV/TV and porosity, ε = 1-BV/TV, can be obtained. **Note 4**: ISM models do not have statistical variability. The mean values of BS and BV in the NBTS models showed deviations of less than 3% over samples of 3 replicates.

NRP increases. In fact, in the interval shown ($200 \leq NRP \leq 800$) the BS/BV ratio decreased linearly for the Tb.Th values considered (square correlation coefficient, $0.99352 \leq r^2 \leq 0.99677$).

It should be noticed that the information obtained from Fig. 8a can also be deduced from Fig. 7a. Therefore, Fig. 7a and 8a contain all the information necessary to build any of the new models since

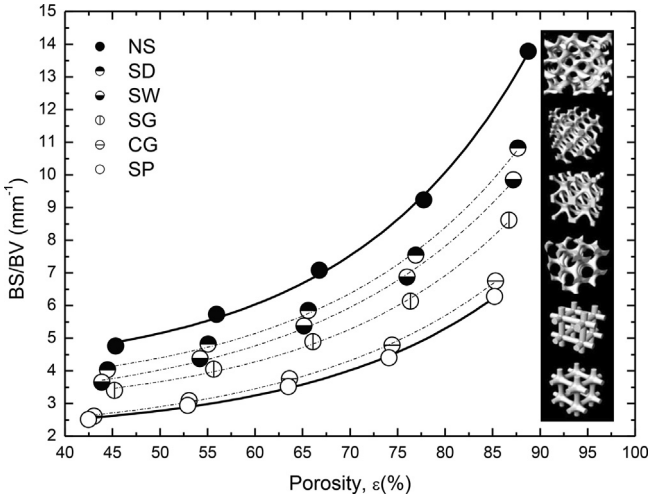

Fig. 6. Specific surface area (BS/BV) *versus* porosity (ε = 1-BV/TV; dimensionless by definition) for the ISM models. The scaffolds, whose geometry is also shown, fitted an exponential growth behaviour. The NS model has the highest BS/BV ratio (see the text for further explanations).

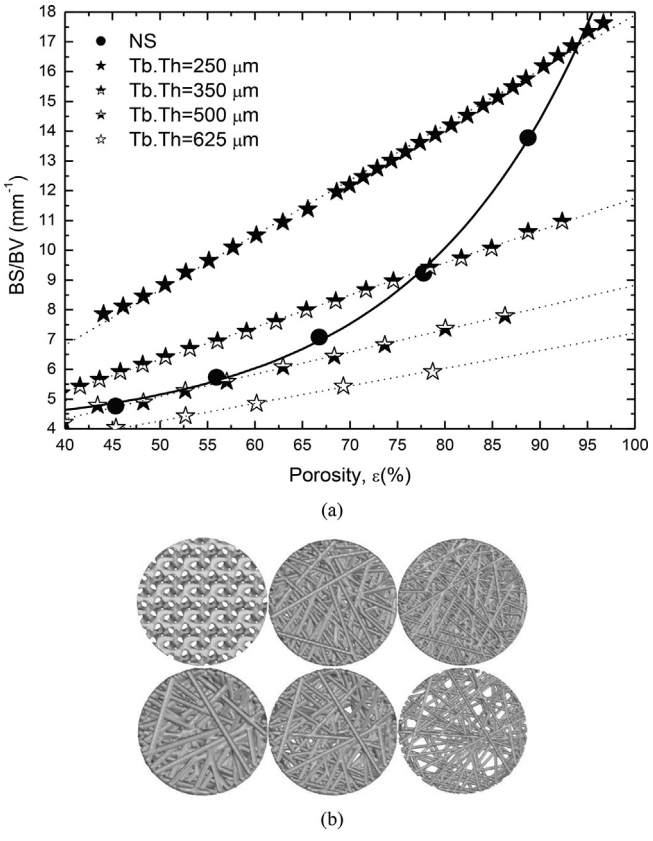

Fig. 7. a) Specific surface area (BS/BV) *versus* porosity (ε = 1-BV/TV; dimensionless by definition) for the new models NBTS as compared to the implicit model NS. b) Microarchitecture detail of some NBTS and NS cylindrical models (top view, see the text for further explanations).

once the specific surface and porosity is selected (Fig. 7a), the trabecular thickness and the number of random points necessary for their design are also fixed (Fig. 8a). As an example, Fig. 8 b shows (top line) how the microstructure of the model having 250 μm of Tb.Th changes as the number of random points moves to 200, 500 and 800. These modifications change the BS/BV ratio and

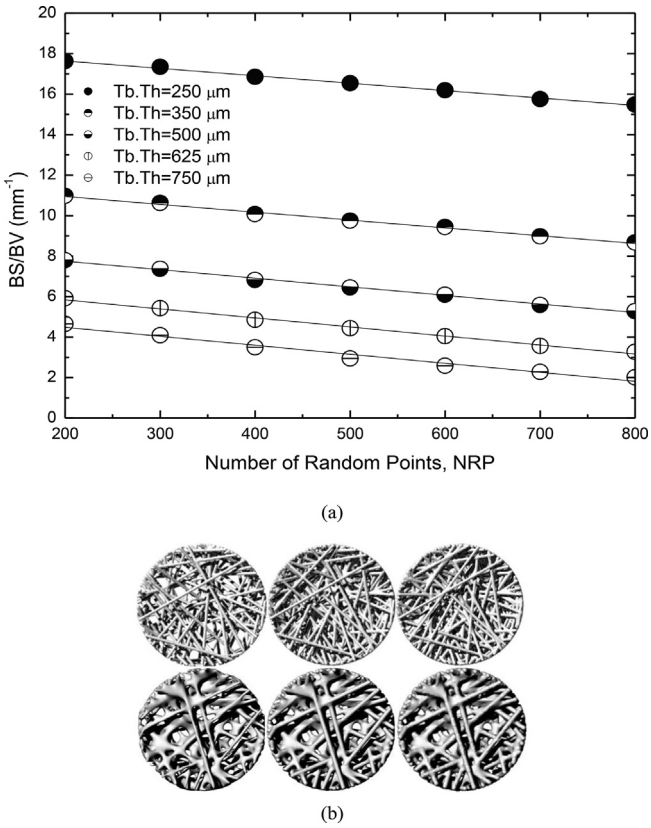

Fig. 8. a) Specific surface area (BS/BV) *versus* the number of random points (NRP) for some selected trabecular thickness values (Tb.Th). b) Top line: Microstructure changes of a sample made with 250 μm of Tb.Th but different NRP (200, left; 500, middle; 800, right). Down line: Microstructure changes of a sample made with 250 μm of Tb.Th and 200 NRP but with different surface curvatures (sample cube size = 0 (left); 0.1 (middle); 0.2 (right)). See the text for further explanations.

porosity of the model, accordingly (16.78 mm^{-1}, 93.21 %; 14.76 mm^{-1}, 83.92 %; 12.87 mm^{-1}, 74.22 %). It should be highlighted that the models can be further designed to have different surface curvatures by rounding off and smoothing the contact areas where several trabeculae meet together (see also Fig. 1d). As an example, Fig. 8b shows (down line) the effect of increasing curvatures (sample cube size = 0, 0.1 and 0.2, according to software *Cocoon*^{TM}) on the microstructure of one of these models (Tb.Th = 250 μm and NRP = 200). In this case, the new curvature requirements adjusted the BS/BV ratio and the porosity of the model, accordingly (15.47 mm^{-1}, 86.86 %; 14.73 mm^{-1}, 85.36 %; 14.12 mm^{-1}, 83.19 %).

3.2. Characterization of mechanical properties

Fig. 9a shows the main trends observed for the evolution of the relative Young's modulus (E_r) against the porosity (ε) of the studied models. It is observed that for the ISM models that had the best and the worst BS/BV ratio (i.e., the NS and the SP, respectively; see, Fig. 6), the Young's modulus decreased linearly in the interval of the interested porosity (i.e., 0.45 < ε < 0.85), with squared correlation coefficients of 0.99892 and 0.99925, respectively. Moreover, the NS model showed higher values of E_r than the SP model in the studied interval, with decreasing differences between both models as the porosity increased. The other studied ISM models (i.e., SD, SW, SG and CG; see, Fig. 6) have not been included in Fig. 9a for clarity's sake due to their intermediate behaviour. Additionally, the new NBTS models showed similar linear behaviour as the ISM models. However, these models were clearly affected by

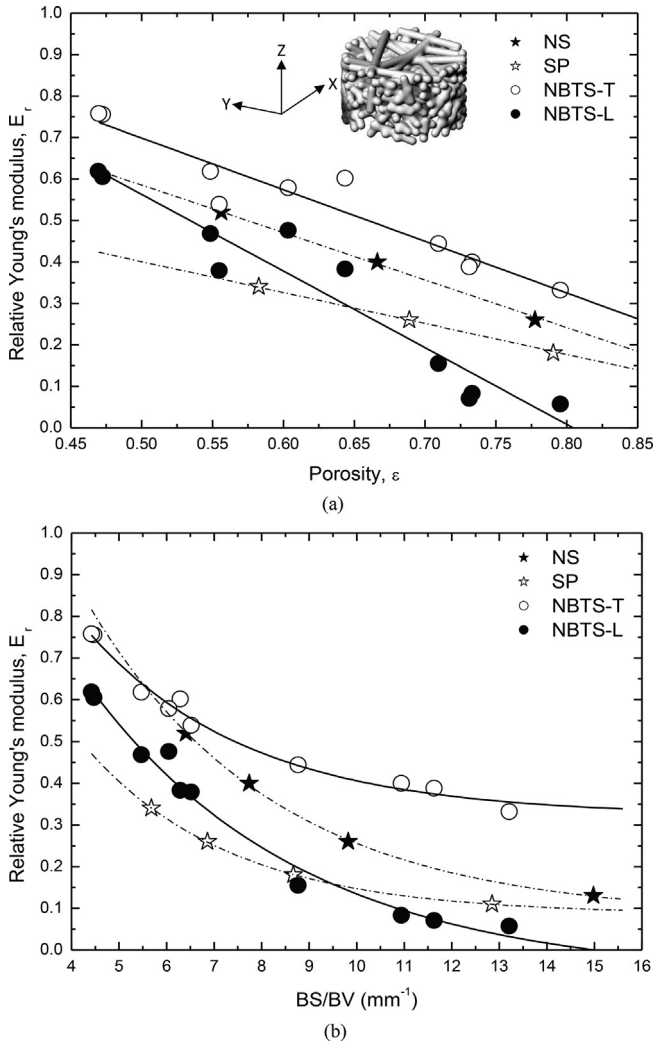

Fig. 9. a) Relative Young's modulus (E_r; dimensionless by definition) *versus* porosity (ε = 1-BV/TV; dimensionless by definition); and, b) Relative Young's modulus (E_r) *versus* specific surface area (BS/BV), for the new NBTS models (two ISM models, NS and SP, are included for comparison purposes). See the text for further explanations.

their inherent design anisotropy. For example, the Youngs' modulus in the transversal section (sample coded NBTS-T) was higher than in the longitudinal one (sample coded NBTS-L), being the differences between them higher for higher porosity values. It is interesting to observe that the Young's modulus of the new NBTS model, in the transversal section, while being higher than the ones measured for the NS model, had a similar decreasing slope as that model (i.e., -1.25 ± 0.13 and -1.15 ± 0.03, respectively). This is due to the similar trabecular arrangement that is observed in the new models in their transversal section (random radial trabecular disposition) as compared to the one observed along whatever symmetry axis in the NS model (see, Fig. 5c).

Fig. 9b complements the observations of Fig. 9a. In this case, the relative Young's modulus has been related to the specific surface area of the models (see also, Figs. 6 and 7 which relate specific surface area and porosity for a better comprehension). In this Fig. 9b, the mathematical functionality between E_r and BS/BV was of the exponential decay ($y = y_0 + A_1 \cdot e^{-x/t_1}$), with squared correlation coefficients comprised in the range $0.98442 \leq r^2 \leq 0.99989$. This figure clearly shows that for BS/BV > 13 mm^{-1}, the E_r tends to zero for the new NBTS models at least in the longitudinal direction (i.e., for $\varepsilon > 0.8$; see, Fig. 9a). Moreover, the NS model showed higher E_r values than the new models in the longitudinal direction (NBTS-L) when tested, at constant BS/BV ratio, in the interval 4.5 < BS/BV (mm^{-1}) < 15. However, for BS/BV > 5.5 mm^{-1} the new models in the transversal section (NBTS-T) had higher E_r values than the NS model, when they were both tested at the same BS/BV ratio.

3.3. Characterization of fluid flow properties

Fig. 10 shows the correlations observed between the permeability (k) and the porosity (ε) for some representative implicit surface models as to compare the new NBTS models. In this figure, only the NS (similar to SW) and the SP (similar to CG) models have been represented because the SG (not shown for the sake of clarity, and similar to SD) showed an intermediate behaviour between that observed for the NS and the SP models. In general, these ISM models fit well in exponential growth trends (i.e., $K = K_0 + e^{\varepsilon/\varepsilon_0}$) with squared correlation coefficients (r^2) of 0.99981 (SP), 0.99992 (SG) and 0.98605 (NS). On the other hand, the new NBTS models showed (at constant trabecular thickness) linear trends with positive correlation coefficients ($0.97662 \leq r \leq 0.9991$). In this case, linear trends moved from the right to the left, with a slowly decreasing slope, as Tb.Th increased. This figure, in fact, shows that the permeability/porosity area covered by the ISM models can be also covered by the new NBTS models by an appropriate selection of Tb.Th and NRPs (note that NRPs increases for each linear trend from top to down along the fitting line).

Additionally, Fig. 11 shows the correlations observed between the tortuosity (τ) and the porosity (ε) for some representative ISM models (SW, SP and SG) as to compare the new NBTS models. This figure gives a more clear microstructural picture than that observed in Fig. 10, where both, permeability and porosity are, in fact, macrostructural features of the studied material models. In this sense, Fig. 11 gives a better idea of how the models are built internally at the microstructural level. To clarify, only three ISM models have been included in Fig. 11, and these are compared to the new NBTS models. The selected ISM models were the SW, the SP and the SG because they showed the lowest, the medium and the highest tortuosity values, respectively. These models fitted linear trends with negative correlation coefficients ($-0.99929 \leq r \leq -0.98003$) and increasing slopes in the following order, SW < NS > SP ≅ CG < SG ≅ SD. On the other hand, the new NBTS models nearly showed the same slope in the interval of

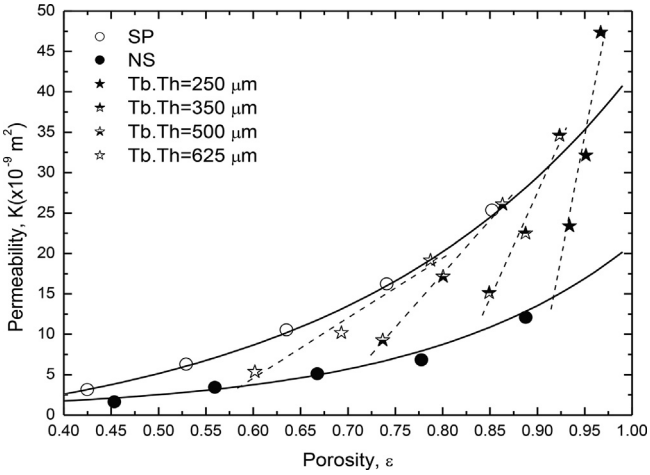

Fig. 10. Permeability (k) *versus* porosity (ε = 1-BV/TV; dimensionless by definition) for some ISM representative models (NS and SP) as compare to the new NBTS models with different trabecular thickness (Tb.Th). See the text for further explanations.

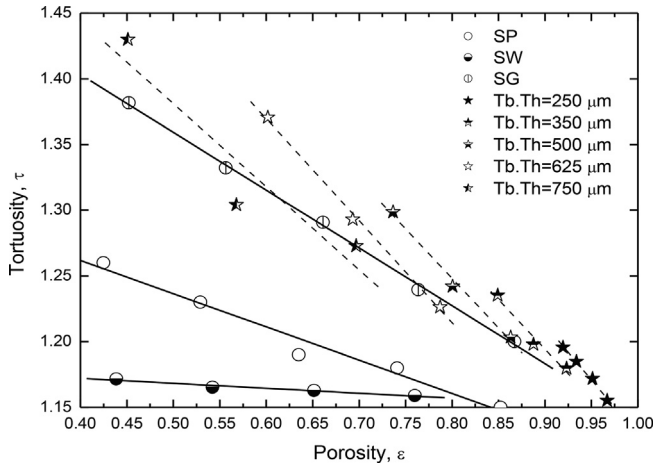

Fig. 11. Tortuosity (τ; dimensionless by definition) *versus* porosity (ε = 1-BV/TV; dimensionless by definition) for some ISM representative models (SW, SP and SG) as compared to the new NBTS models with different trabecular thickness (Tb.Th). See the text for further explanations.

$250 \leq$ Tb.Th(μm) ≤ 625, with negative correlation coefficients in the range of $-0.99592 \leq r \leq -0.98363$. Moreover, Fig. 11 clearly shows that the new NBTS models allowed the improvement of tortuosity far beyond the highest value allowed by the implicit surface model SG by, again, selecting appropriate values of Tb.Th and NRPs (note that NRPs increases for each linear trend, in this figure, from down to top along the fitting line).

Finally, Fig. 12 shows the correlations observed between tortuosity (τ) and permeability (k) for the same models studied in Fig. 11. This representation gives more information about the clear differences observed between the studied ISM models as compared to the new NBTS proposed models. This figure, where the linear trends were again confirmed, clearly shows that the new NBTS models extend beyond the influence area of tortuosity/permeability values covered by the studied ISM models. In this figure, the linear trends pictured for each Tb.Th value also contain information about the NRPs, these increased from right to left along the fitting line.

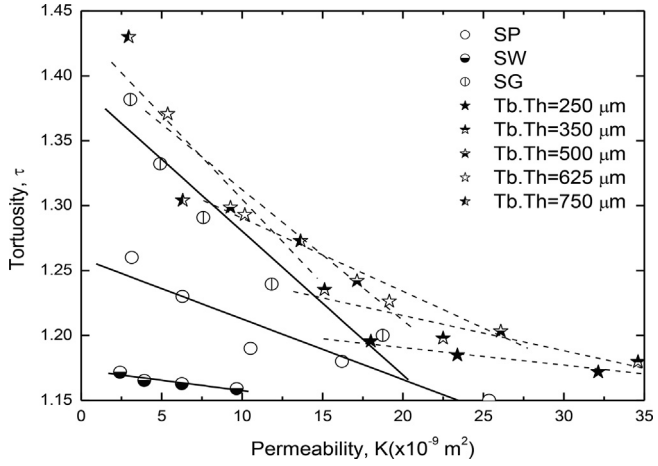

Fig. 12. Tortuosity (τ; dimensionless by definition) *versus* permeability (k) for some ISM representative models (SW, SP and SG) as compared to the new NBTS models with different trabecular thickness (Tb.Th). See the text for further explanations.

4. Discussion

In this study a computer aided design novel method has been applied to design new bio-inspired 3D porous scaffolds that mimic the mechanical and fluid properties of cancellous bone. It is known that cell adhesion, migration and, ultimately, local tissue formation are improved by increasing the bone surface ratio (i.e., BS/TV and BS/BV) of the scaffold by acting on both, trabecula's interconnection and surface modulation [12–17]. In this sense, it is expected that the new proposed microstructure should also favour bone cells penetration and nutrients mass transport in service conditions [1–6]. Considering this, several observations can be made from our results. For example, Figs. 6 and 7 show that for bone like porous scaffolds with optimum porosity, i.e., $0.7 < \varepsilon < 0.9$, similar to that encountered in human trabecular bone [35,36], the new model designed with Tb.Th of 250 μm presented greater BS/BV ratio than any of the other studied ISM models. Additionally, Fig. 8a shows that by adjusting the number of random points (NRP) and the diameter of the generating cylinders (i.e., Tb.Th) it is possible to design bio-inspired bone-like models with specific surface area values showing porosities and pore's interconnectivity features (see Fig. 8b) similar to those shown by natural trabecular bone [13–17,37]. In this sense, the possibility of designing new models with controlled curvature trabecular connections (see, Fig. 8b) is of special interest because cells adhere and behave differently to concave/convex substrates [13,19] and, consequently, an exact control of the concave/convex surface ratio should further optimize scaffolds for bone tissue restoration. In addition, as BS/BV, ε, NRP and Tb.Th are interrelated factors (see, Figs. 6-8a), the Fig. 9-a-b show that models designed with both higher values of Tb.Th and NRPs, i.e. lower ε and BS/BV ratio, also show higher normalized Young's modulus E_r, showing in consequence that by an appropriate design procedure and selection of indices it is even possible to produce porous scaffolds with predefined anisotropic mechanical properties. For example, in our case, as the NBTS models were designed with higher trabecular concentration in the transversal (T) rather than the longitudinal (L) stress applied direction, so was the Young's modulus, (i.e., $1.16 \leq E_p^T\,(GPa) \leq 2.64$; $0.17 \leq E_p^L$(-GPa) ≤ 2.15), in the interval of interest porosity (i.e., $0.45 < \varepsilon < 0.85$; see Fig. 9), values which were in any case in agreement with other previous studies [38–40]. In consequence, it can be concluded that the new design methodology, presented in this study, is suitable to create bio-inspired porous scaffolds with similar trabecular bone indices as natural trabecular bone that also have a higher specific surface area and stiffness than those obtained for equivalent ISM's scaffolds. In addition, the possibility that the new method offers to control the curvature and the smoothing of contact trabecular surfaces (see, Fig. 1 and Fig. 8.b) is a factor of real value to promote cellular adhesion and tissue formation in more demanding *in vivo* applications. Moreover, the new method allows, if necessary, the design of scaffolds with higher stiffness in the transversal stress direction by selecting set points properly oriented to generate more longitudinal trabeculae. This freedom to select different groups of points is, in fact, one of the main advantages of the method. For example, by distributing random points into separate groups, the directionality of the trabeculae (cylinder connections) and consequently the bionic feature of the implant design can be easily controlled because the connections between different groups of points located in space (A, B, C, etc.) can be forced, thereby improving the mechanical and/or rheological properties of the implant along the preferred orientations, even mimicking the anisotropic properties of any bone implant site.

Obviously, all these fitting changes will at the end determine not only mechanical but also fluidic properties of the scaffold along different symmetry directions. This is in fact what the permeability

and tortuosity results show (see, Figs. 10-12). For example, Fig. 10 shows that the NBTS models were able to cover the permeability interval, $5 < k\left(x10^{-9}m^2\right) < 50$, in the interval of porosities, $0.6 < \epsilon < 0.98$, with trabeculae in the interval, $250 < Tb.Th(\mu m) < 625$. Additionally, Fig. 10 shows that despite the permeability of the scaffolds increases with porosity, as expected, it decreases, at constant porosity, for increasing BS/BV ratios (i.e., for decreasing Tb.Th values; see also, Fig. 7). In this sense, the results clearly show that porosity is not the only factor affecting permeability (i.e., nutrients mass transport) and that other microstructural indices affecting fluid flow surface friction such as pore size, pore interconnectivity, trabecular size and trabecular orientation should also be considered [21–23,27,33]. The optimization of all these factors will tune, at the end, the environment through which nutrients and metabolic wastes will be able to diffuse [6,12,13]. In any case, the permeability results obtained for the new NBTS scaffolds were better than those obtained for the ISM models and are agreeable to those found in other studies for natural trabecular bone [41–45].

Similar trends can be deduced from our tortuosity results (see, Figs. 11 and 12). The new NBTS scaffolds showed higher tortuosity values than their equivalent ISM models. This is so because the NBTS models have an irregular distribution of pore channels that affect the ratio between the actual path length connecting pores to their Euclidean distance. On the other hand, the ISM models have an aligned regular distribution of pore channels that favour a more free fluid flow pass (see, Figs. 3 and 4). In any case, our results, which were in agreement to other literature studies for natural trabecular bone [46], clearly show that tortuosity increases for each model with the reduction of their porosity (Fig. 11) and consequently with the reduction of their permeability (Fig. 12). Therefore, tortuosity also depends on design indices such as Tb.Th and NRPs and the dependency is of a direct proportional relation.

Despite cell responses on tortuous scaffolds is still rarely quoted in the literature, some authors have proposed that tortuous channels favour the growth rate of osteoblasts [47]. In this sense, it is clear that the osteogenic behaviour of the new NBTS models will depend ultimately on the appropriate selection of their microstructural design indices. Moreover, as the proposed methodology can create scaffolds with different microstructural features in different regions of the same volume of interest, it is possible to create complex human trabecular bone scaffolds by reverse engineering 3D reconstruction of tomography medical images (Fig. 2). Thus, the STL file can be used to print the 3D scaffold with biocompatible or bioinert material by additive manufacturing technology. The scaffolds can be further treated with specific cells and nutrients for specific bone tissue engineering applications.

Finally, it should be mentioned that the *in vitro* and the *in vivo* behaviour of the new bio-inspired porous bone-like scaffolds were out of the scope of the present research because, on their own, both studies are appropriate objectives for another deeply and necessary future research, similar to the one the authors did with other equally designed porous bone-like scaffolds that showed appropriate *in vitro* and *in vivo* behaviour [48].

5. Conclusion

The present study shows that computational aided design allows the creation of bio-inspired bone-like tissue scaffolds with controlled complex micro and macro architecture. The specific design method proposed allows the design of implantable structures that mimick natural bone properties. The results have shown that the computed mechanical and fluid flow properties of the novel bone tissue scaffolds directly depend on the microstructural features of the porous structure, being the total porosity, the bone surface area and the direction of trabecula the main factors to control, where these factors depend on microstructural design indices like Tb.Th, NRPs, the rounding and the smoothing of surface transitions and the preferential direction of trabecula. All these design parameters are easily controlled during the design computation of the model which additionally can adopt whatever external shape is needed. Moreover, the method allows the design of scaffolds with internal connected volumes that have different design indices and consequently continuous but graded properties between different areas, which further increase their possibilities of use.

In particular, the results obtained clearly showed that the new NBTS models had the following advantages: a) models designed with Tb.Th of 250 μm and similar porosity to that encountered in human trabecular bone ($0.7 < \varepsilon < 0.9$) presented greater specific surface ratio than any of the other studied ISM models (Figs. 6 and 7); b) models mimicking the histomorphometry of an equivalent ISM model always showed improved properties for specific surface area, mechanical stiffness (Figs. 8 and 9), permeability (Fig. 10) and tortuosity (Figs. 11 and 12); and c) the new methodology of design can create different models, with distinct histomorphometric features, in different regions of the same volume of interest, and connect them to create a continuous complex and anisotropic human-like trabecular bone; this is simply not possible with ISM models.

6. Data availability

The raw/processed data required to reproduce these findings cannot be shared at this time due to technical or time limitations but they will be provided upon request to the authors, if needed.

7. Statement of significance

A new computer-aided-design method has been used to develop novel bio-inspired three-dimensional bone-like scaffolds. These scaffolds have an internal anisotropic and interconnected porous microstructure with a highly specific surface area and controllable surface curvatures. The final mechanical and fluid mass transport properties of the new scaffolds can be tuned during the initial design stage of the bone-like histomorphometric microstructure. The method can be applied to whatever external volume shape to modify its inside with different bone-like porous microstructures. In this sense, the external volume shapes can be reconstructed from computed tomography medical images. The new scaffolds could be manufactured by 3D printing technologies.

Data availability

Data will be made available on request.

Declaration of Competing Interest

The authors declare that they have no known competing financial interests or personal relationships that could have appeared to influence the work reported in this paper.

Acknowledgements

The authors thank funding projects DPI2016-77768-R (Ministerio de Economía y Competitividad, Spain) and 2017SGR253 (Agència de Gestiò d'Ajuts Universitaris i de Recerca, Generalitat de Catalunya, Spain). M.D. Vlad also thanks the research project Contract-No. 29033/28.12.2016 financed by Grigore T. Popa University of Medicine and Pharmacy from Iasi.

References

[1] R.J. O'Keefe, J. Mao, Bone tissue engineering and regeneration: from discovery to the clinic – an overview, Tissue Eng. Part B Rev. 17 (6) (2011) 389–392, https://doi.org/10.1089/ten.teb.2011.0475.

[2] Y. Liu, J. Lim, S.H. Teoh, Review: development of clinically relevant scaffolds for vascularised bone tissue engineering, Biotechnol. Adv. 31 (5) (2013) 688–705, https://doi.org/10.1016/j.biotechadv.2012.10.003.

[3] S. Bose, M. Roy, A. Bandyopadhyay, Recent advances in bone tissue engineering scaffolds, Trends Biotechnol. 30 (10) (2012) 546–554, https://doi.org/10.1016/j.tibtech.2012.07.005.

[4] D.W. Hutmacher, J.T. Schantz, C.X. Lam, K.C. Tan, T.C. Lim, State of the art and future directions of scaffold-based bone engineering from a biomaterials perspective, J. Tissue Eng. Regen. Med. 1 (4) (2007) 245–260, https://doi.org/10.1002/term.24.

[5] B.M. Willie, A. Petersen, K. Schmidt-Bleek, A. Cipitria, M. Mehta, P. Strube, J. Lienau, B. Wildemann, P. Fratzl, G. Duda, Designing biomimetic scaffolds for bone regeneration: why aim for a copy of mature tissue properties if nature uses a different approach?, Soft Matter 6 (2010) 4976–4987, https://doiorg/10.1039/C0SM00262C.

[6] S.J. Hollister, Porous scaffold design for tissue engineering, Nat. Mater. 4 (2005) 518–524, https://doi.org/10.1038/nmat1421.

[7] Y. Khan, M.J. Yaszemski, A.G. Mikos, C.T. Laurencin, Tissue engineering of bone: material and matrix considerations, J. Bone Joint Surg. Am. 90 (1) (2008) 36–42, https://doi.org/10.2106/JBJS.G.01260.

[8] C.N. Kelly, A.T. Miller, S.J. Hollister, R.E. Guldberg, K. Gall, Design and structure–function characterization of 3D printed synthetic porous biomaterials for tissue engineering, Adv. Healthcare Mater. 7 (7) (2018) 1701095, https://doi.org/10.1002/adhm.201701095.

[9] C. Ghayor, F.E. Weber, Osteoconductive microarchitecture of bone substitutes for bone regeneration revisited, Front. Physiol. 9 (2018) 960, https://doi.org/10.3389/fphys.2018.00960.

[10] F.E. Weber, Reconsidering osteoconduction in the era of additive manufacturing, Tissue Eng. Part B 5 (2019) 375–386, https://doi.org/10.1089/ten.TEB.2019.0047.

[11] C. Ghayor, I. Bhattacharya, F.E. Weber, The optimal microarchitecture of 3D-printed β-TCP bone substitutes for vertical bone augmentation differs from that for osteoconduction, Mater. Des. 204 (2021), https://doi.org/10.1016/j.matdes.2021.109650 109650.

[12] Z. Wang, C. Wang, C. Li, Y. Qin, L. Zhong, B. Chen, Z. Li, H. Liu, F. Chang, J. Wang, Analysis of factors influencing bone ingrowth into three-dimensional printed porous metal scaffolds: a review, J. Alloys Compd. 717 (2017) 271–285, https://doi.org/10.1016/j.jallcom.2017.05.079.

[13] X. Wang, S. Xu, S. Zhou, W. Xu, M. Leary, P. Choong, Y.M. Xie, Topological design and additive manufacturing of porous metals for bone scaffolds and orthopaedic implants: a review, Biomaterials 83 (2016) 127–141, https://doi.org/10.1016/j.biomaterials.2016.01.012.

[14] S. Wu, X. Liu, K.W. Yeung, C. Liu, X. Yang, Biomimetic porous scaffolds for bone tissue engineering, Mater. Sci. Eng. R Rep. 80 (2014) 1–36, https://doi.org/10.1016/j.mser.2014.04.001.

[15] A.A. Zadpoor, Bone tissue regeneration: the role of scaffold geometry, Biomater. Sci. 3 (2015) 231–245, https://doi.org/10.1039/C4BM00291A.

[16] C.M. Bidan, K.P. Kommareddy, M. Rumpler, P. Kollmannsberger, P. Fratzl, J.W. Dunlop, Geometry as a factor for tissue growth: towards shape optimization of tissue engineering scaffolds, Adv. Healthcare Mater. 2 (1) (2013) 186–194, https://doi.org/10.1002/adhm.201200159.

[17] M. Rumpler, A. Woesz, J.W. Dunlop, J.T. van Dongen, P. Fratzl, The effect of geometry on three-dimensional tissue growth, J. R. Soc. Interface 5 (27) (2008) 1173–1180, https://doi.org/10.1098/rsif.2008.0064.

[18] S.M. Giannitelli, D. Accoto, M. Trombetta, A. Rainer, Current trends in the design of scaffolds for computer-aided tissue engineering, Acta Biomater. 10 (2) (2014) 580–594, https://doi.org/10.1016/j.actbio.2013.10.024.

[19] D.W. Hutmacher, M. Sittinger, M.V. Risbud, Scaffold-based tissue engineering: rationale for computer-aided design and solid free-form fabrication systems, Trends Biotechnol. 22 (2004) 354–362, https://doi.org/10.1016/j.tibtech.2004.05.005.

[20] W. Sun, B. Starly, A. Darling, C. Gomez, Computer-aided tissue engineering: application to biomimetic modelling and design of tissue scaffolds, Biotechnol. Appl. Biochem. 39 (1) (2004) 49–58, https://doi.org/10.1042/BA20030109.

[21] S.B. Blanquer, M. Werner, M. Hannula, S. Sharifi, G.P. Lajoinie, D. Eglin, J. Hyttinen, A.A. Poot, D.W. Grijpma, Surface curvature in triply-periodic minimal surface architectures as a distinct design parameter in preparing advanced tissue engineering scaffolds, Biofabrication 9 (2) (2017), https://doi.org/10.1088/1758-5090/aa6553 025001.

[22] D.J. Yoo, Porous scaffold design using the distance field and triply periodic minimal surface models, Biomaterials 32 (31) (2011) 7741–7754, https://doi.org/10.1016/j.biomaterials.2011.07.019.

[23] S.C. Kapfer, S.T. Hyde, K. Mecke, C.H. Arns, G.E. Schröder-Turk, Minimal surface scaffold designs for tissue engineering, Biomaterials 32 (29) (2011) 6875–6882, https://doi.org/10.1016/j.biomaterials.2011.06.012.

[24] Z. Chen, Z. Su, S. Ma, X. Wu, Z. Luo, Biomimetic modeling and three-dimension reconstruction of the artificial bone, Comput. Methods Programs Biomed. 88 (2) (2007) 123–130, https://doi.org/10.1016/j.cmpb.2007.08.001.

[25] W. Sun, B. Starly, J. Nam, A. Darling, Bio-CAD modeling and its applications in computer-aided tissue engineering, Comput. Aided Des. 37 (11) (2005) 1097–1114, https://doi.org/10.1016/j.cad.2005.02.002.

[26] A. Okabe, B. Boots, K. Sugihara, S.N. Chiu, Spatial tessellations: concepts and applications of Voronoi diagrams, 2nd Ed., John Wiley & Sons Ltd, Baffins Lane, England, 2000.

[27] S. Gómez, M.D. Vlad, J. López, E. Fernández, Design and properties of 3D scaffolds for bone tissue engineering, Acta Biomater. 42 (2016) 341–350, https://doi.org/10.1016/j.actbio.2016.06.032.

[28] G. Wang, L. Shen, J. Zhao, H. Liang, D. Xie, Z. Tian, C. Wang, Design and compressive behavior of controllable irregular porous scaffolds: based on Voronoi-tessellation and for additive manufacturing, ACS Biomater. Sci. Eng. 4 (2) (2018) 719–727, https://doi.org/10.1021/acsbiomaterials.7b00916.

[29] D.J. Cornelissen, A. Faulkner-Jones, W. Shu, Current developments in 3D bioprinting for tissue engineering, Curr. Opin. Biomed. Eng. 2 (2017) 76-82 10.1016/j.cobme.2017.05.004.

[30] S.H. Park, C.S. Jung, B.H. Min, Advances in three-dimensional bioprinting for hard tissue engineering, Tissue Eng. Regen. Med. 13 (2016) 622–635, https://doi.org/10.1007/s13770-016-0145-4.

[31] A. Syahrom, M.R.A. Kadir, J. Abdullah, A. Öchsner, Permeability studies of artificial and natural cancellous bone structures, Med. Eng. Phys. 35 (6) (2013) 792–799, https://doi.org/10.1016/j.medengphy.2012.08.011.

[32] A.L. Olivares, E. Marsal, J.A. Planell, D. Lacroix, Finite element study of scaffold architecture design and culture conditions for tissue engineering, Biomaterials 30 (30) (2009) 6142–6149, https://doi.org/10.1016/j.biomaterials.2009.07.041.

[33] R.P. Widmer, S.J. Ferguson, A comparison and verification of computational methods to determine the permeability of vertebral trabecular bone, Proc. Inst. Mech. Eng. H 227 (2013) 617–628, https://doi.org/10.1177/0954411912462814.

[34] E.A. Nauman, K.E. Fong, T.M. Keaveny, Dependence of intertrabecular permeability on flow direction and anatomic site, Ann. Biomed. Eng. 27 (1999) 517–524, https://doi.org/10.1114/1.195.

[35] S. Gómez, M.D. Vlad, J. López, M. Navarro, E. Fernández, Characterization and three-dimensional reconstruction of synthetic bone model foams, Mater. Sci. Eng. C 33 (6) (2013) 3329–3335, https://doi.org/10.1016/j.msec.2013.04.013.

[36] D. Ulrich, B. Rietbergen, A. Laib, P. Rüegsegger, The ability of three-dimensional structural indices to reflect mechanical aspects of trabecular bone, Bone 25 (1999) 55–60, https://doi.org/10.1016/S8756-3282(99)00098-8.

[37] H. Montazerian, E. Davoodi, M. Asadi-Eydivand, J. Kadkhodapour, M. Solati-Hashjin, Porous scaffold internal architecture design based on minimal surfaces: A compromise between permeability and elastic properties, Mater. Des. 126 (2017) 98–114, https://doi.org/10.1016/j.matdes.2017.04.009.

[38] D. Wu, P. Isaksson, S.J. Ferguson, C. Persson, Young's modulus of trabecular bone at the tissue level: A review, Acta Biomater. 78 (2018) 1–12, https://doi.org/10.1016/j.actbio.2018.08.001.

[39] T.M. Keaveny, W.C. Hayes, A 20-year perspective on the mechanical properties of trabecular bone, J Biomech Eng. 115 (4B) (1993) 534–542, https://doi.org/10.1115/1.2895536.

[40] C. Öhman-Mägi, O. Holub, D. Wu, R.M. Hall, C. Persson, Density and mechanical properties of vertebral trabecular bone—A review, JOR Spine 4 (4) (2021) e1176.

[41] M.J. Grimm, J.L. Williams, Measurements of permeability in human calcaneal trabecular bone, J. Biomech. 30 (7) (1997) 743–745, https://doi.org/10.1016/S0021-9290(97)00016-X.

[42] J.C. Teo, S.H. Teoh, Permeability study of vertebral cancellous bone using micro-computational fluid dynamics, Comput. Methods Biomech. Biomed. Engin. 15 (4) (2012) 417–423, https://doi.org/10.1080/10255842.2010.539563.

[43] H. Montazerian, M. Zhianmanesh, E. Davoodi, A.S. Milani, M. Hoorfar, Longitudinal and radial permeability analysis of additively manufactured porous scaffolds: Effect of pore shape and porosity, Mater. Des. 122 (2017) 146–156, https://doi.org/10.1016/j.matdes.2017.03.006.

[44] M.R. Dias, P.R. Fernandes, J.M. Guedes, S.J. Hollister, Permeability analysis of scaffolds for bone tissue engineering, J. Biomech. 45 (6) (2012) 938–944, https://doi.org/10.1016/j.jbiomech.2012.01.019.

[45] P.G. Coelho, P.R. Fernandes, H.C. Rodrigues, Multiscale modeling of bone tissue with surface and permeability control, J. Biomech. 44 (2) (2011) 321–329, https://doi.org/10.1016/j.jbiomech.2010.10.007.

[46] T. Zeiser, M. Bashoor-Zadeh, A. Darabi, G. Baroud, Pore-scale analysis of Newtonian flow in the explicit geometry of vertebral trabecular bones using lattice Boltzmann simulation, Proc. Inst. Mech. Eng. H 222 (2) (2008) 185–194, https://doi.org/10.1243/09544119JEIM261.

[47] M.M.C.G. Silva, L.A. Cyster, J.J.A. Barry, X.B. Yang, R.O.C. Oreffo, D.M. Grant, C.A. Scotchford, S.M. Howdle, K.M. Shakesheff, F.R.A.J. Rose, The effect of anisotropic architecture on cell and tissue infiltration into tissue engineering scaffolds, Biomaterials 27 (35) (2006) 5909–5917, https://doi.org/10.1016/j.biomaterials.2006.08.010.

[48] M.D. Vlad, E. Fernández, S. Gómez, I.C. Ivanov, E.V. Şindilar, I. Poeată, A.Ş. Iencean, M. Butnaru, E.R. Avădănei, J. López, Novel titanium-apatite hybrid scaffolds with spongy bone-like micro architecture intended for spinal application: In vitro and in vivo study, Mater. Sci. Eng. C 110 (2020), https://doi.org/10.1016/j.msec.2020.110658 110658.